Proceedings of the ASME 2019 14th International Manufacturing Science and Engineering Conference
MSEC2019
June 10-14, 2019, Erie, PA, USA

MSEC2019-2875

A GRAPH THEORETIC APPROACH FOR NEAR REAL-TIME PREDICTION OF PART-LEVEL THERMAL HISTORY IN METAL ADDITIVE MANUFACTURING PROCESSES

Reza Yavari[a], Kevin D. Cole[a], Prahalad Rao[a,1]

[a]Mechanical and Materials Engineering Department, University of Nebraska-Lincoln, Lincoln, NE 68588-0526, United States

ABSTRACT

The goal of this work is to predict the effect of part geometry and process parameters on the instantaneous spatial distribution of heat, called the heat flux or thermal history, in metal parts as they are being built layer-by-layer using additive manufacturing (AM) processes. In pursuit of this goal, the objective of this work is to develop and verify a graph theory-based approach for predicting the heat flux in metal AM parts. This objective is consequential to overcome the current poor process consistency and part quality in AM. One of the main reasons for poor part quality in metal AM processes is ascribed to the heat flux in the part. For instance, constrained heat flux because of ill-considered part design leads to defects, such as warping and thermal stress-induced cracking. Existing non-proprietary approaches to predict the heat flux in AM at the part-level predominantly use mesh-based finite element analyses that are computationally tortuous – the simulation of a few layers typically requires several hours, if not days. Hence, to alleviate these challenges in metal AM processes, there is a need for efficient computational thermal models to predict the heat flux, and thereby guide part design and selection of process parameters instead of expensive empirical testing. Compared to finite element analysis techniques, the proposed mesh-free graph theory-based approach facilitates layer-by-layer simulation of the heat flux within a few minutes on a desktop computer. To explore these assertions we conducted the following two studies: (1) comparing the heat diffusion trends predicted using the graph theory approach, with finite element analysis and analytical heat transfer calculations based on Green's functions for an elementary cuboid geometry which is subjected to an impulse heat input in a certain part of its volume, and (2) simulating the layer-by-layer deposition of three part geometries in a laser powder bed fusion metal AM process with: (a) Goldak's moving heat source finite element method, (b) the proposed graph theory approach, and (c) further comparing the heat flux predictions from the last two approaches with a commercial solution. From the first study we report that the heat flux trend approximated by the graph theory approach is found to be accurate within 5% of the Green's functions-based analytical solution (in terms of the symmetric mean absolute percentage error). Results from the second study show that the heat flux trends predicted for the AM parts using graph theory approach agrees with finite element analysis with error less than 15%. More pertinently, the computational time for predicting the heat flux was significantly reduced with graph theory, for instance, in one of the AM case studies the time taken to predict the heat flux in a part was less than 3 minutes using the graph theory approach compared to over 3 hours with finite element analysis. While this paper is restricted to theoretical development and verification of the graph theory approach for heat flux prediction, our forthcoming research will focus on experimental validation through in-process sensor-based heat flux measurements.

Keywords: Additive Manufacturing, Thermal Modeling, Heat Flux, Graph Theory.

1 Introduction

1.1 Objective

The goal of this work is to understand the effect of process parameters and part design (part geometry) on the instantaneous spatial distribution of heat, also called the heat flux or thermal history, in metal parts as they are being built (printed) layer-by-layer using additive manufacturing (AM) processes [1]. As a step towards this goal, the objective of this work is to develop and verify a graph theory-based approach for predicting the heat flux in metal AM parts.

Shown in Figure 1(a) is the laser powder bed fusion (LPBF) AM process in which layers of metal powder are rolled or raked across a build plate and selectively melted using a laser to form

[1] Corresponding author. Tel.: +01-402-472-3458; fax: +01-402-472-1465. *E-mail address:* rao@unl.edu

the part. Figure 1 (b) shows a schematic of a directed energy deposition (DED) metal AM process, wherein a stream of powder material is directed onto a substrate via nozzles. The powder is melted through the thermal action of a laser. By translating the nozzle relative to the substrate in the horizontal and vertical planes, a desired part geometry is built layer-upon-layer [2].

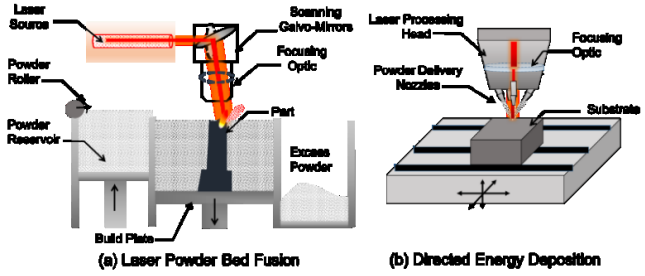

Figure 1: The schematic of the laser powder bed fusion (LPBF) and blown powder directed energy deposition (DED) metal AM processes.

1.2 Motivation for Thermal Modeling in Metal AM

Metal AM processes, such as LPBF and DED offer significant advantages over conventional subtractive and formative manufacturing processes including design flexibility and shorter lead times [3-5]. However, poor process consistency and inferior part quality currently afflict metal AM processes [6-11]. Given the uncertainty in part quality, precision-oriented strategic sectors, such as aerospace and biomedical, are reluctant to deploy metal AM processes for making safety-critical parts. The three main process-related reasons that impede the quality of metal AM parts are [12]:

(1) Inconsistency in the as-built microstructure, termed as microstructural heterogeneity [13, 14].
(2) Porosity formation, which includes the case of poor consolidation of the material called lack-of-fusion porosity due to insufficient input energy to melt the material, as well as, vaporization of the powder material due to excessive input energy called pinhole porosity [15, 16].
(3) Deviations in the as-built geometry from its intended design due to distortion. At the part-level, other defects, beside distortion, include cracking and delamination of layers.

The aforementioned flaws are largely governed by thermal phenomena, specifically, the magnitude and direction of heat flow in the part as it is being built – called the heat flux or thermal history [12, 17]. To explain further, the salient thermal phenomena in LPBF and DED, stratified by the various energy-part-process interaction zones, are represented in Figure 2 [18]. The thermal phenomena depicted in Figure 2 encompass complex conductive, convective, and radiative heat transfer interactions between the part, energy source, material, and chamber (powder, as well as gas). These thermal aspects in AM, which govern the heat flux in the part, are in turn a function of the material, part design and the process parameters, such as the power and velocity settings of the laser used for melting the material [19].

Statistical experimentation methods to obtain the desired geometry and microstructure in AM will involve building test parts by adjusting process parameters, followed by destructive materials characterization. Such a statistical designed experiments-based approach is prohibitively expensive, and may not be viable in metal AM given the small batch sizes, vast parameter space (there are over 50 variables in LPBF alone), and the slow nature of AM processes compared to conventional manufacturing [20, 21]. Furthermore, owing to the tight coupling of the part design, material properties, and parameters to the heat flux, a set of parameters optimized for a particular part geometry and material are not readily transferable to a new part design and material [8].

Therefore, as emphasized by several researchers, to ensure part quality in metal AM, it is imperative to understand and explain the following intertwined links in the LPBF process chain through quantitative modeling [22-27]: Part Design, Process Parameters, and Material Characteristics → Heat Flux → Microstructure and Geometry Flaws [28-31].

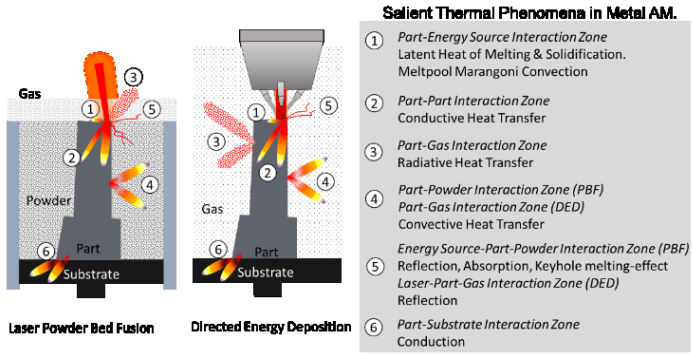

Figure 2: The salient heat transfer modes in LPBF and DED encompassing complex interactions amongst the part, material, energy source, and environment (surrounding inert gas).

The bourgeoning need for a formal framework based on fundamental understanding of the thermal physics of the process to guide the design of the AM parts and parameter selection is practically illustrated in Figure 3, which shows a biomedical knee implant built by the authors using the LPBF process [32]. This part has a feature called an overhang whose underside is not supported. To prevent the part from collapsing under its own weight, supports were automatically built under the overhang feature by the native software on the LPBF machine. Nonetheless, after the build, the overhang area was found to have coarse-grained microstructure, distortion and poor surface finish, which makes the implant potentially unsafe for clinical use.

Such defects, also reported in the literature by other researchers, result from the heat being constrained in the overhang section [33-36]. The reason for the constrained heat in the overhang section is hypothesized due to the low thermal conductivity of the surrounding metal powder, and the thin cross-sectional area of the supports. Through accurate and computationally efficient thermal simulations that can predict the effect of process conditions and part design on heat flux, occurrence of defects, such as geometric deformation and microstructure heterogeneity can be minimized without extensive empirical optimization [37].

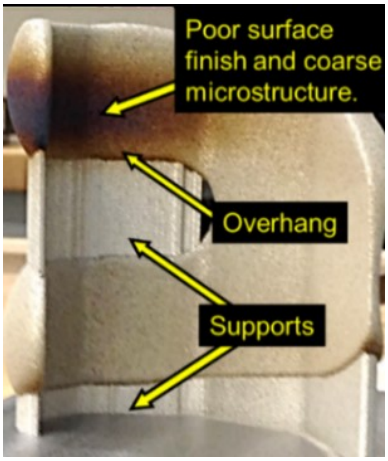

Figure 3. LPBF knee implant with an overhang feature shows poor surface finish and coarse microstructure.

1.3 Novelty and Advantages of the Proposed Graph Theory Approach

Accurate quantitative modeling approaches based on finite element (FE) analyses have been successfully developed and applied for understanding the thermal aspects of AM at the part-level as summarized in Ref. [11, 12, 38-40]. However, these pioneering non-proprietary approaches reported in the published literature are computationally expensive, with simulation of a few deposited layers amounting to many hours, if not days [41, 42]. For example, Chou *et al.,* reported that the computation time for thermomechanical analysis for a 6 mm cuboid shape exceeds 92 hours [41]. Hence, newer computationally efficient approaches are needed to approximate the heat flux given different part designs and process parameters. In the context of FE-based modeling we note that certain commercial, proprietary approaches, such as Autodesk Netfabb and Ansys 3DSim have leveraged adaptive meshing principles to drastically reduce the computational time. However, the underlying mathematics of these commercial software applications is proprietary [39, 43]. Within the context of heat flux prediction, the advantages in using the graph theoretic approach to solve the heat diffusion equation, are two-fold:

Reduced computational burden due to elimination of mesh-based analysis

Instead of solving the heat diffusion equation for each element through element birth-and-death techniques as in finite element (FE) analysis, we track the heat flux in the part in terms of nodes of a planar graph projected onto its geometry. Our efforts in verifying results from the graph theoretic approach with the FE analysis, described in Sec. 4.2, leads us to infer that, a significant portion of the computation effort in FE analysis is consumed by the meshing of elements, and simulation of the birth-and-death process to mimic material deposition in AM. The graph theoretic approach circumvents the need for meshing, and as a result, the computation time for simulation of AM processes can be considerably reduced compared to existing, non-proprietary FE analysis-based approaches.

Elimination of matrix inversion steps required to solve the heat diffusion equation.

While FE analysis rests on matrix inversion steps to solve the heat diffusion equation for each of the thousands of elements, the graph theoretic method instead relies on the more computationally tractable matrix multiplication operations to obtain the eigenvectors ($\boldsymbol{\phi}$) and eigenvalues ($\boldsymbol{\Lambda}$) of the graph Laplacian ($\mathbf{L}$) (to be discussed subsequently in Sec. 3), which greatly reduces the computational burden.

By reducing the computational time in predicting the heat flux to minutes, as opposed to hours, estimating the geometric distortion and microstructural evolution govern the heat flux becomes considerably more tractable. Furthermore, the near real-time predictions of heat flux made possible through the proposed approach, lays the foundation for feed-forward control of microstructure and geometry through theoretical understanding of the thermal history as opposed to data-driven machine learning and analytics.

1.4 Organization of the Paper

The rest of this paper is organized as follows. The literature concerning the FE-based thermal modeling of metal AM processes at the part-level is outlined in Sec. 2. Next, the graph theoretic approach for solving the heat equation is described in Sec. 3, wherein we show that the eigenvectors ($\boldsymbol{\phi}$) and eigenvalues ($\boldsymbol{\Lambda}$) of the Laplacian matrix ($\mathbf{L}$) solve the heat diffusion equation, which governs heat flux in AM. We dedicate Sec. 4 of this paper to the verification of the graph theory approach through the following two studies: (1) verifying the heat flux trends obtained from graph theory with exact Green's functions-based analytical method, and finite element analysis for an elementary cuboid geometry, and (2) comparing the heat flux trends derived using graph theory approach for three part geometries in a LPBF simulation scenario with the heat flux trends obtained by implementing Goldak's moving heat source FE analysis solution, and Autodesk's Netfabb software. This paper closes in Sec. 1 with conclusions and avenues for future work.

2 Prior Research in Finite Element Modeling in Metal AM Processes

It is beyond the scope of this paper to provide an in-depth exposition of the vast and mature area of finite element (FE) analysis in AM, which is the *de facto* means to solve the heat diffusion equation described later in Sec. 3 as applied to metal AM. The reader is referred to the recent book by Denlinger *et al.* [39] which comprehensively details the approach, challenges, and practical application concerning FE-based thermomechanical analysis in AM. Comprehensive review articles on part-level thermal modeling in AM with the finite element method in metal AM have been recently published by Luo and Zhao [37], Bandyopadhyay and Traxel [38], and DebRoy, *et al.* [11]. These articles provide an in-depth review the strategies that have been advanced by researchers to reduce the computational burden of FE analysis in AM; a summary of these is provided below.

(1) Adaptive meshing and element activation schema

Researchers have simplified the meshing process, such as consolidating layers into blocks or super-layers using an adaptive mesh refinement and coarsening strategy [42]. The key idea is that certain areas of the part, where the cross-section and boundaries change sharply have finer mesh while the rest of the part may has a coarser mesh. Further, researchers in metal AM have adapted two main approaches to simulate the deposition of the material in the FE framework [44]. In the first approach, called the inactive element method, elements are incrementally added when the melting process is initiated. Though the inactive approach closely mimics the AM processes, it is challenging to implement because the number of elements increases as the part grows.

The second technique is called the quiet element method, wherein the part is meshed *a priori*, but only elements in the current layers and those below are thermally active. The properties of the elements in the succeeding layers are deliberately altered to have no thermal effect. To reduce the computational burden, commercial approaches, such as Netfabb (Autodesk) have taken two tacks:

(i) adaptive mesh refinement of the part, such that certain areas have large or coarser nodes; and
(ii) using a hybrid meshing approach combining quiet and inactive meshing schema. Such a hybrid element activation schema was pioneered by Michaleris and is reported to be implemented in Netfabb [44].

(2) Simplification of the process physics

As first described in Figure 2, the main heat transfer mechanisms in the process are:

(i) conductive heat losses at the part and substrate level, wherein the heat on the top surface travels through the solidified layers in the bottom, and further through the substrate;
(ii) radiative heat loss at the top surface to the process chamber;
(iii) loss due to convection at the boundary of the printed part and the surrounding powders; and
(iv) latent heat involved at the melt-pool zone as the material state changes from solid to liquid, and back to solid again on cooling.

Incorporating all these heat transfer mechanisms in a model will inordinately increase its computational burden. Consequently, researchers resort to simplifications, such as: ignoring latent heat effects from the melt-pool; maintaining static material properties, such as a constant heat conduction rate, density and specific heat; and, ignoring the radiative heat losses into the chamber and the convective heat losses into the surrounding powder by assuming the part to be completely insulated. Some of these simplifications have been shown to have a significant effect on the prediction accuracy of cooling rates [37].

(3) Simplifying the part geometry, energy source, and powder bed-related conditions.

Researchers seek to reduce the computational burden by simplifying the part geometry, such as simulating only one half of a symmetric part, or considering deposition in the form of super-layers [40]. Furthermore, the behavior of the energy source is also simplified by assuming heating of an entire layer at once, or in terms of rectilinear hatches, as opposed to complicated island type scanning. The thermal models can also incorporate strategies to simplify the effect of the energy source by approximating the shape of the beam, e.g., assuming Gaussian, ellipsoidal, and tophat shapes. Mesh-free approaches in AM are being explored, such as electric network type modeling schema introduced by Hoelzle *et al.* [45], and discrete finite difference modeling by Zohdi and Ganeriwala [46, 47].

From a graph theoretic perspective, a review paper by Solomon [48] discusses discrete differential operators that arise from partial differential equations (PDEs) such as the heat equation; it shows that the Laplacian matrix constructed from a uniformly-spaced grid gives a solution to the heat equation. However, if the grid is not equally spaced, the relationship to the correct solution of the heat equation is not clear. In a study of geometric surface smoothing, Belkin *et al.* [49] assert that their discrete Laplacian matrix approaches the continuous Laplacian in the limit as the grid become sufficiently fine, even if the grid pattern is non-uniform. Their algorithm includes multiplicative factor $1/\varepsilon^2$ where ε which is the size of the neighborhood of influence for nearby grid points. In a study of image smoothing, Zhang and Hancock use randomly-assigned node locations to construct a discrete Laplacian matrix and subsequently to solve the heat equation [50]. In closing this section, we note that the proposed graph theoretic approach is distinct from the mesh-free methods developed for peridynamics of systems undergoing dynamic cracking [51, 52], and it is also different from spectral collocation methods where splines provide an *a priori* functional form of the solution as part of a standard matrix-inversion process [53, 54].

3 The Graph Theoretic Approach for Approximating the Heat Flux in AM

3.1 Assumptions of the Graph Theoretic Model

To keep the development brief, the following simplifying assumptions are applied to the graph theoretic approach.

- *Heat transfer-related assumptions.* The thermal properties of the material are static, in that, they do not change as the material changes state from particulate matter to a liquid (meltpool formation), and then back to a solid. In other words, the latent heat of melting and solidification is ignored. The heat loss due to vaporization, and material composition and density changes due to mass transfer are also not considered. Likewise, the radiative effects from the top surface of the part are not accounted.
- *Energy source-related assumptions.* The laser is considered a moving point heat source, i.e., the beam diameter and shape, and subsequent diffusion of the laser on the powder

bed surface are not accounted. It is assumed that the laser rays are completely absorbed in the topmost layer and are not repeatedly reflected by the powder. Hence, effects such as key-hole melting, and variations in thermal absorptivity contingent on powder packing density on the powder bed are ignored.

- *Powder bed-related assumptions.* There is only one single part in the build plate at a given time, hence there is no heat exchanged with other parts. Lastly, the powder bed is considered to be at the same temperature as the chamber, and that the packing density of the powder bed remains static.

These assumptions can be relaxed to provide a more comprehensive model, which will be pursued in later works by the authors.

2 The Heat Diffusion Equation and its Connection to Heat Flux in AM

As stated previously, the objective of this work is to develop and apply a graph theoretic approach to predict the temperature history in metal AM parts. To realize this objective, we solve the heat diffusion equation,

$$\rho c_p \frac{\partial \mathrm{T}}{\partial t} - k\left(\frac{\partial^2}{\partial x^2}+\frac{\partial^2}{\partial y^2}+\frac{\partial^2}{\partial z^2}\right)\mathrm{T} = \mathrm{E}_V \qquad (1)$$

In Eqn. (1), T is the instantaneous temperature at a location $\{x, y, z\}$ at time t. The AM process parameters are captured in the energy density, E_V, which is the energy supplied by the laser to the top layer to melt a unit volume of material per second; $\mathrm{E}_V = \frac{P}{h_t \cdot d \cdot l}$ [W/mm^3], where P is the laser power in [W], h_t is the width of the laser track or hatch [mm], d the layer height [mm], and l the length melted in one second [mm]. The material properties are encapsulated in the following terms: density ρ [kg/m^3], specific heat c_p [J/(kg·K)], and thermal conductivity k [W/(m·K)].

From the AM perspective, the term $\partial \mathrm{T}/\partial t$ is analogous to the rate of change of temperature at a particular point in the part referenced by its spatial coordinates $\{x, y, z\}$ as it is heated by a moving energy source, e.g., a laser in LPBF, while being consolidated layer-upon-layer. Solving the heat equation results in the instantaneous temperature $\mathrm{T}(x, y, z, t)$ at a time t for a Cartesian spatial coordinate $\{x, y, z\}$. The temporal map of $\mathrm{T}(x, y, z, t)$, i.e., the trace of the temperature T at the location $\{x, y, z\}$ over time, gives the temperature history in the part for that location.

The graph theory approach to the solution of the heat diffusion equation relies upon two approximations. First, the source term, E_V, in Eqn. (1) is replaced by an initial temperature distribution, for which the portion of the AM part that is scanned by the laser is assigned an elevated temperature to represent, for example, the metal fusion temperature. The heat equation is solved repeatedly, again and again, following each laser scan. Specifically, consider a spatial point $\{x, y, z\}$ during the AM process, immediately after a laser scan is completed, the heat diffusion equation to be solved takes the form,

$$\frac{\partial \mathrm{T}}{\partial t} - \alpha\left(\frac{\partial^2}{\partial x^2}+\frac{\partial^2}{\partial y^2}+\frac{\partial^2}{\partial z^2}\right)\mathrm{T} = 0$$
$$\mathrm{T}(x, y, z, t=0) = \mathrm{T}_o(x, y, z) \qquad (2)$$

In Eqn. (2), T_0 is the initial condition and $\alpha = k/(\rho c_p)$ is the thermal diffusivity. The solution of the above heat diffusion equation describes the evolving temperature in the AM part in the time period between one laser scan and the next. After a layer is completely processed, the build platen is lowered, and a new layer of powder is deposited over the top of the previous layer. When the new layer is deposited and scanned by the laser, an update to the computational domain is required along with a new initial condition. These updates necessitate a re-computation of the heat equation. This rationale is valid even when a more granular laser hatch-by-hatch evolution of the process is simulated. To explain further, the new computational domain includes the newly-fused layer of metal powder at an elevated temperature on top of the previously-fused metal whose initial temperature is the end point of the previous temperature computation. Just as the part is created layer-by-layer (or hatch-by-hatch), the temperature solution is computed in many small discrete increments of time.

A mathematical premise key to the graph theory approach is that the spatial derivatives in the above continuum heat diffusion equation, Eqn. (1) and (2), can be replaced by suitable discrete approximations, and the continuously varying temperature T can be replaced by a vector of discrete temperatures **T** at M sampled nodal points in the domain of the part. The discrete form of the heat diffusion equation, with vectors in bold typeface may be written as,

$$\frac{\partial \mathbf{T}}{\partial t} + \alpha \mathbf{L}\mathbf{T} = 0 \qquad (3)$$

Note the sign change in Eqn. (3), as the Laplacian matrix **L** from graph theory is defined with sign opposite to that of the continuous spatial derivatives present in the continuous heat equation (Eqn. (2)). If the above discrete form of the heat diffusion equation is applied to a uniformly-spaced grid of nodal points, a discrete Laplacian matrix can be constructed to reproduce the well-known finite-difference approximation [55].

The foregoing is important in the context of the present work because the finite-difference approximation has been shown, in the limit as the inter-nodal spacing approaches zero, to be exact [55]. Although the present work uses non-uniform node spacing, the point to be made here is that the level of approximation in the graph theoretic approach is related to that of the well-known finite-difference method. The details of the specific Laplacian matrix used in the present work are discussed in the next section; the mathematical proof of the graph theory-based solution to the heat equation, Eqn. (2) is provided in the Appendix.

3.2 Steps in Predicting the Heat Flux in AM using Graph Theory

The approach has the following four steps, as pictorially shown in Figure 4, and in Figure 5 as a flowchart diagram. The steps are as follows, with respect to the LPBF process:

(1) Obtain the geometry of a part and convert it to a set of discrete nodes. Slice the part into layers and hatches. Record the position of each node, in terms of its Cartesian $\{x, y, z\}$ coordinates, and the layer and hatch in which the node is located.

(2) Construct a network graph from the discrete nodes sampled in Step (1). In this step, each of the nodes is connected to other nodes within an ε neighborhood.

(3) (a) Simulate the heating of a layer, hatch-by-hatch, and diffuse the heat through the network graph constructed on the nodes sampled in the part, noting that only the nodes in the current layer and below are active, and (b) after the heat diffuses through the part, simulate the deposition of a new layer on top. Step 3 is repeated until the part is built.

(4) At each iteration of Step 3, the heat at each node at each time step is recorded in terms of the temperature vector **T.**

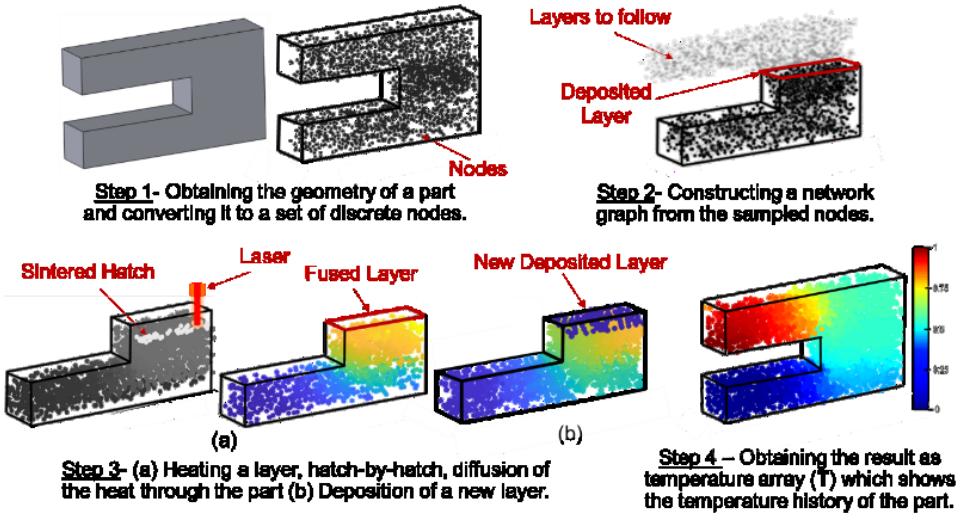

Figure 4. The four steps in the spectral graph theoretic approach used to estimate the heat flux in the part layer-by-layer. Here we show an embodiment of the laser powder bed fusion (LPBF) process.

Figure 5. The flowchart of four steps in the graph theoretic approach in context of LPBF process

Step 1: Obtain the geometry of a part and converting it to a set of discrete nodes

Process parameters and the part geometry are declared in this step. The part is sliced into layers, representative of the layer thickness, and a fixed number (M) of spatial locations are randomly sampled in each layer. In the later steps, the heat flux through the part is observed and stored (recorded) at these M fixed spatial locations, termed nodes.

The random sampling of the nodes is done to reduce the computational burden of the approach. The number of nodes sampled is contingent on the geometry of the part, in this work (Sec. 4.2) , a density of 5 nodes per mm^3 provided a sufficiently good approximation (relative error < 15%) to the heat flux estimated with a moving heat source solution obtained through FE analysis [56, 57].

Step 2: Network graph construction

In graph theory, a concept of discrete mathematics, a graph consists of nodes and the edges that connect them [58]. Here nodes are spatial points sampled in the part and the edges are the links among the nodes. We begin by constructing a graph over the set of M nodes sampled in Step 1. The aim is to connect a pair of nodes π_i and π_j within an ε neighborhood. Consider, $c_i = \{x_i, y_i, z_i\}$ as the location of the node π_i, and $c_j = \{x_j, y_j, z_j\}$ as the location of the node π_j, then the weight of the edge connecting node π_i and π_j is expressed in mathematical terms below, with a Gaussian radial basis function,

$$a_{ij} = \begin{cases} e^{-\frac{(c_i - c_j)^2}{\sigma^2}}, & (c_i - c_j)^2 \le \epsilon \\ 0. & (c_i - c_j)^2 > \epsilon \end{cases} \quad (4)$$

where $(c_i - c_j)^2$ is the square of the distance between nodes π_i and π_j. In this work, the term ϵ is akin to the radius of a sphere within which one node is connected to its neighbors, and σ is the standard deviation of the pairwise distances, $(c_i - c_j)^2$.

We note that Eqn. (4) embodies the Gaussian law in that, if two nodes are closer, their weight will be proportionally larger. We further note that a_{ij} takes a value between 0 and 1. Next, we place each element a_{ij} on the i^{th} row and j^{th} column of the adjacency matrix **A**. Essentially, the element i^{th} row and j^{th} column of **A** relates to strength of the edges connecting the nodes π_i and π_j.

$$\mathbf{A} = [a_{ij}] \quad (5)$$

The matrix **A** is a symmetric M × M matrix because $a_{ij} = a_{ji}$. The next step involves computing the degree d_i of a node π_i, i.e., the aggregate of the strength of the edges that are connected to the node π_i. The degree of node π_i is computed by summing the i^{th} row of the Adjacency matrix **A.**

$$d_i = \sum\nolimits_{\forall j} a_{ij} \quad (6)$$

From the degree of node d_i, the Laplacian l_{ij} at node *i* is defined as follows,

$$l_{ij} \stackrel{\text{def}}{=} d_i - a_{ij} \quad (7)$$

We note that $\sum_{\forall j} l_{ij} = 0$. If the diagonal degree matrix **D** is formed from d_i's as follows,

$$\mathbf{D} = \begin{bmatrix} d_1 & \cdots & 0 \\ \vdots & \ddots & \vdots \\ 0 & \cdots & d_{\mathrm{M}} \end{bmatrix} \quad (8)$$

then given the adjacency matrix **A**, the discrete Laplacian **L** can be cast in matrix form as,

$$\mathbf{L} \stackrel{\text{def}}{=} (\mathbf{D} - \mathbf{A}) \quad (9)$$

Finally, the Eigen spectra of the Laplacian **L** is computed as follows,

$$\mathbf{L}\boldsymbol{\phi} = \boldsymbol{\phi}\boldsymbol{\Lambda} \quad (10)$$

Where $\boldsymbol{\phi}$ are the eigenvectors and $\boldsymbol{\Lambda}$ are the eigenvalues of **L**. We note that **L** is a real, diagonally dominant symmetric matrix, with positive diagonal entries, and negative off-diagonal entries. Due to these properties **L** falls under the category of a Stieltjes matrix, and has non-negative eigenvalues ($\boldsymbol{\Lambda}$) and orthogonal eigenvectors ($\boldsymbol{\phi}$) [58].

Step 3: (a) Heating a layer, hatch-by-hatch, diffusion of the heat through the part, and (b) deposition of a new layer.

In Step 3(a), the heat from the laser is applied to the top-most layer in the form of hatches. The magnitude of heat applied is E_V [W/m^3]. Where the time taken to fuse a hatch is considered infinitesimal compared to the taken to that build the whole layer or the time it takes the bed to be lowered and to the recoater to deposit a new layer. The heat diffuses to the rest of the part within the powder bed, and through the substrate in the time (t). As we will show in the forthcoming two sections, the eigenvectors $\boldsymbol{\phi}$ of the Laplacian **L** provide a discrete solution to the heat equation, specifically, if $\boldsymbol{\phi}'$ is the transpose of $\boldsymbol{\phi}$, then the temperature profile observed at a discrete time step t for a node at position (x, y, z) below the top layer is given by the following, the mathematical proof of which is given in Appendix.

$$\mathrm{T}(x, y, z, t) = \boldsymbol{\phi} e^{-\alpha g \boldsymbol{\Lambda} t} \boldsymbol{\phi}' \mathrm{T}_0(x, y, z) \quad (11)$$

Where, T_0 is the initial temperature distribution introduced to simulate laser heating. The material-related factors are contained in the term α [m^2/s] and g is a constant *gain factor* [m^{-2}]. Lastly, we need to account for the heat loss due to convection at the boundary of the powder and part. For this purpose, we demarcate the boundary nodes of the part, and adjust the temperature of the boundary nodes (T_b) using Newton's law of cooling,

$$\mathrm{T}_b = e^{-\tilde{h}(\Delta t)} \left(\mathrm{T}_{bi} - \mathrm{T}_p\right) + \mathrm{T}_p \quad (12)$$

Where, T_p is the temperature of the powder (considered to be equal to the ambient temperature in the environment, T_∞), T_{bi} is the initial temperature of the boundary nodes, T_b is the

temperature of the boundary nodes after convective heat loss and $\tilde{h}$ is the normalized coefficient of convection from part to the surrounding powder (also called the Biot number), and Δt is the dimensionless time between laser scans.

In Step 3(b) which is only applicable to the LPBF process, and not DED, a layer of powder is raked on top of the fused layer. The process repeats through Step 3(a) and (b) until the part is built. At every iteration of Step 3, we estimate the heat flux across layers, and store the resulting temperature of each node $T(x, y, z, t)$, inside a temperature vector $\mathbf{T}$, which eventually in Step 4 represents the temperature history and heat distribution of the whole part.

4 Verification of the Approach

This section is divided into two parts. The first part, described in Sec. 4.1, compares the graph theory approach with the exact Green's function-based analytical solution and finite element solution for heat flux in a simple cuboid geometry [59]. The second part, detailed in Sec. 4.2, applies the graph theory approach for predicting the heat flux to three part designs in a LPBF scenario, the results obtained therefrom are compared with Goldak's FE-based solution, and a commercial implementation (Netfabb) [56, 57].

4.1 Verification of the Graph Theory Approach for a Cuboid Geometry

This section aims to quantify the accuracy of the graph theory heat flux solution by comparison with analytical and finite element solutions for a simple test case. This test case simulates heat diffusion in a cube. The cube is assumed to be insulated on the boundaries (Neumann boundary condition) which results in internal heat dispersion until a steady-state condition is achieved. There is a fixed volume inside the cube which is considered to be momentarily heated for a vanishingly small time. Each edge of this heated volume is half the of the entire cube, meaning the volume of the heated section is one-eighth of the cube. Figure 6 shows the geometry, initial heated region, and the boundary conditions imposed upon the system. Additional details are available in the author's publications and website [59]. The dimension of the cube is taken to be 1 unit.

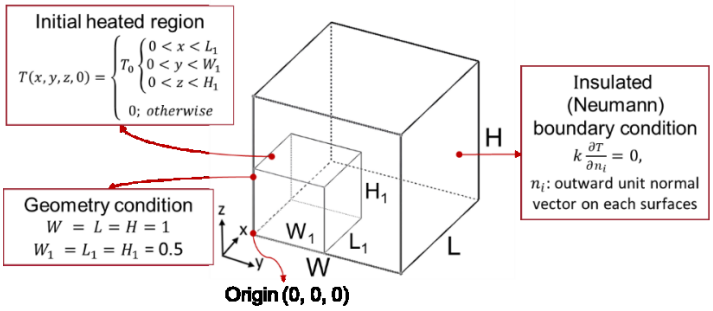

Figure 6. The cube with the initial heating condition and insulated boundaries.

The case of heat diffusion in a cube can be made dimensionless by the following parameterization:

$$\tilde{x} = \frac{x}{L};\ \tilde{y} = \frac{y}{W};\ \tilde{z} = \frac{z}{H};\ \widetilde{W} = \frac{W}{L};\ \widetilde{H} = \frac{H}{L}; \tag{13}$$

$$\tilde{L}_1 = \frac{L_1}{L};\ \widetilde{W}_1 = \frac{W_1}{W};\ \widetilde{H}_1 = \frac{H_1}{H};\ \tilde{t} = \frac{\alpha t}{L^2};\ \tilde{T} = \frac{T}{T_0};$$

Where, L, W and H are the geometrical dimensions of the cube, L_1, W_1 and H_1 are the geometrical dimensions of the heated cube, t is time, α is thermal diffusivity, T_0 is the initial temperature and T is the final temperature. Subsequently, the dimensionless form of the heat equation and boundary value problem for the cube-shape are given by:

$$\frac{\partial^2 \tilde{T}}{\partial \tilde{x}^2} + \frac{1}{\widetilde{W}^2}\frac{\partial^2 \tilde{T}}{\partial \tilde{y}^2} + \frac{1}{\widetilde{H}^2}\frac{\partial^2 \tilde{T}}{\partial \tilde{z}^2} = \frac{\partial \tilde{T}}{\partial \tilde{t}};\ \begin{cases} 0 < \tilde{x} < 1; \\ 0 < \tilde{y} < 1; \\ 0 < \tilde{z} < 1; \end{cases} \tag{14}$$

At boundary i, we impose the Neumann boundary condition,

$$\frac{\partial \tilde{T}}{\partial \tilde{n}_i} = 0, \qquad i = 1, 2, 3, 4, 5, 6 \tag{15}$$

$$T(\tilde{x}, \tilde{y}, \tilde{z}, 0) = \begin{cases} T_0 \begin{cases} 0 < \tilde{x} < \tilde{L}_1 \\ 0 < \tilde{y} < \widetilde{W}_1 \\ 0 < \tilde{z} < \widetilde{H}_1 \end{cases} \\ 0;\ \text{otherwise} \end{cases} \tag{16}$$

Where, $\tilde{n}_i$ is the outward normal vector from each surface of the cube. The dimensionless form of the analytical diffusion is found by the Green's function (Eqn. (17)); see [60] for a full development of the solution).

$$\begin{aligned} T(\tilde{x}, \tilde{y}, \tilde{z}, \tilde{t}) &= \left[\tilde{L}_1 + 2\sum_{m=1}^{\infty} exp\,(-m^2\pi^2\tilde{t})\frac{cos(m\pi\tilde{x})\,sin(m\pi\widetilde{L_1})}{m\pi}\right] \\ &\times \left[\widetilde{W}_1 + 2\sum_{n=1}^{\infty} exp\,(\frac{-n^2\pi^2\tilde{t}}{\widetilde{W}^2})\frac{cos(n\pi\tilde{y})\,sin(n\pi\widetilde{W_1})}{n\pi}\right] \\ &\times \left[\widetilde{H}_1 + 2\sum_{p=1}^{\infty} exp\,(\frac{-p^2\pi^2\tilde{t}}{\widetilde{H}^2})\frac{cos(p\pi\tilde{z})\,sin(p\pi\widetilde{H_1})}{p\pi}\right] \end{aligned} \tag{17}$$

Here, $m\pi$, $n\pi$ and $p\pi$ are eigenvalues along the x, y and z directions, respectively. The steady state is considered the moment that observation points reach to an equal temperature up to the fourth decimal point. The heat flux is observed at two observation points inside the cube as follows: Point 1 (0.25H, 0.25L, 0.25W) and Point 2 (0.75H, 0.75L, 0.75W). The heat diffusion trends at Point 1 and 2 from the initial time step to steady state convergence are shown in Figure 7.

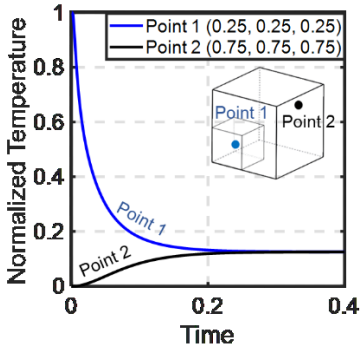

Figure 7. Analytical diffusion at observation point 1: {0.25, 0.25, 0.25} and observation point 2: {0.75, 0.75, 0.75} from the origin.

a. Comparison of the Analytical and Graph Theory Solutions

To compare the accuracy of the graph theory approach with the analytical solution (Figure 7), we conduct the analysis in three steps as shown in Figure 8. In this section we also study the effect of number of nodes and their connection structure on the convergence accuracy of the approach.

Step 1: *Generation of Nodes.*

The whole part is transformed into a set of 91,000 discrete nodes. We randomly sampled different number of nodes from these 91,000 nodes as shown in Figure 8 to study the effect of the number of nodes on the accuracy of the graph theoretic solution. Since the heated volume is one-eighth of the total volume of the cube, we ensure that the number of nodes in the heated subsection is exactly one-eighth of the total nodes.

Each node takes the character of its location, i.e. the nodes which are in the heated subsection take the high-temperature value (equal to 1, which is the highest in normalized temperature range) and the nodes that are outside the heated subsection are set at the low-temperature value (equal to 0, which is the lowest in normalized temperature range) at the initial time step.

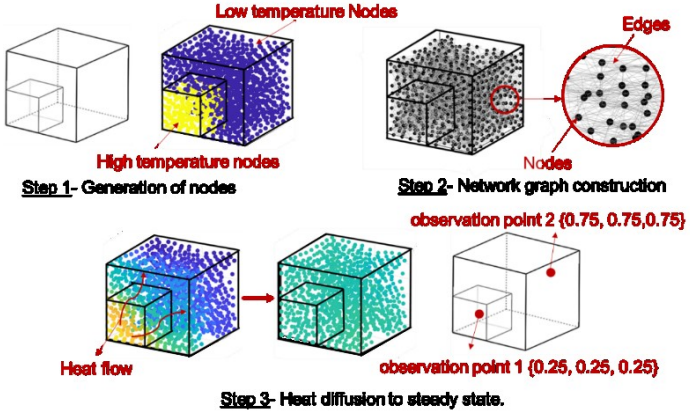

Figure 8. The three steps towards the error calculation and verification with the analytical method.

Step 2: *Network Graph Construction*

In this step, the selected nodes are used to construct a network graph based on their spatial coordinates and neighborhood distance (ε) which is stored in the adjacency matrix as described in Sec. 3.2. Based on the total number of selected nodes and analytical diffusion time, a specific neighboring distance (ε) is required to set the neighboring area for each node. Each node is connected to approximately 20, 80, 300 and 600 neighboring nodes in Case 1, 2, 3 and 4, respectively, as reported in Table 1.

Selecting a higher number of nodes implies a larger adjacency matrix size and requires longer computational time. The computational time corresponds to converting the part to set of discrete nodes and building adjacency matrix which in this work is implemented on a desktop computer with an Intel® Core™ i7-6700 CPU @3.40GHz, 32GB RAM. Table 1 shows the neighborhood distance (ε), adjacency matrix (A) size and graph construction computational time in each case.

Step 3: *Heat Diffusion to Steady State*

The heat diffuses through the graph network until it reaches a steady state condition. We consider the same two observation points, Point 1 at {0.25, 0.25, 0.25} and Point 2 at {0.75, 0.75, 0.75}. The steady state condition is achieved when both observations have the equal temperature up to the fourth decimal point; thermal diffusivity (α), which corresponds the material properties in the graph theory method was considered equal to 1 unit (m^2/s). Figure 9(a) compares the trend of heat diffusion computed using graph theory for Case 2 with the analytical solution. The symmetric mean absolute percent error (SMAPE), defined below in Eqn. (18) is used to quantify the error, where t is the time step and e is the absolute error. Figure 9(b) shows the trends of the SMAPE for the four different cases. Although increasing the number of nodes reduces the error, it leads to longer computational time.

Table 1 delineates the SMAPE and total computational time of the process based on the different number of nodes, from which it is evident even with the sparsest node condition (80 nodes in a cube of 1 × 1 × 1 unit), the error is less than 10%.

$$\text{SMAPE} = \frac{100\%}{\text{n}} \sum_{\forall t} e(t)$$
$$e(t) = \frac{|\,\text{Analytical (t)} - \text{Graph Theoretic(t)}|}{(\text{Analytical (t)} + \text{Graph Theoretic(t)})} \quad (18)$$

Table 1. Details of Graph Theory Heat Diffusion Experiment in a Cube (1 × 1 × 1 unit)

Case	Total number of selected nodes (cold: heated)	Neighbourhood distance (ε) [mm]	Network graph construction time [seconds]	Total graph theoretic solution computational time [seconds]	SMAPE (Error)
1	80 (10: 70)	0.55	0.94	0.97	10%
2	800 (100: 700)	0.37	1.41	1.55	7%
3	4,000 (500: 3,500)	0.31	20.78	38.14	5%
4	8,000 (1,000: 7,000)	0.28	163.33	236.64	3%

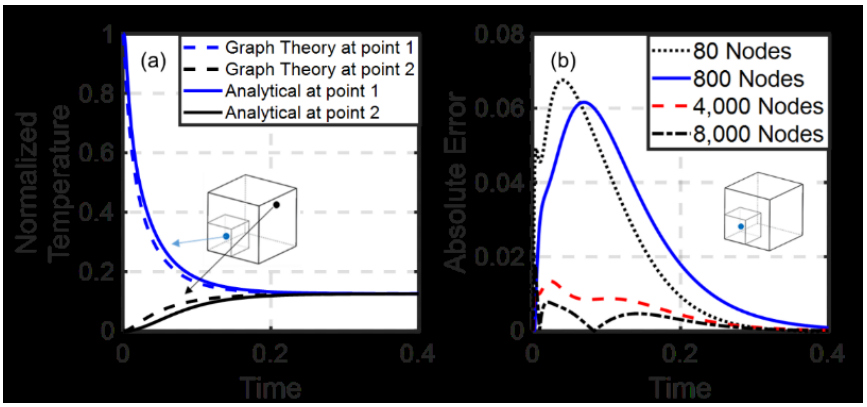

Figure 9. (a) Comparison of the heat diffusion trend between graph theory and analytical method (experiment 2 with 800 selected nodes). (b) absolute error comparison for different amount of nodes at observation point 1.

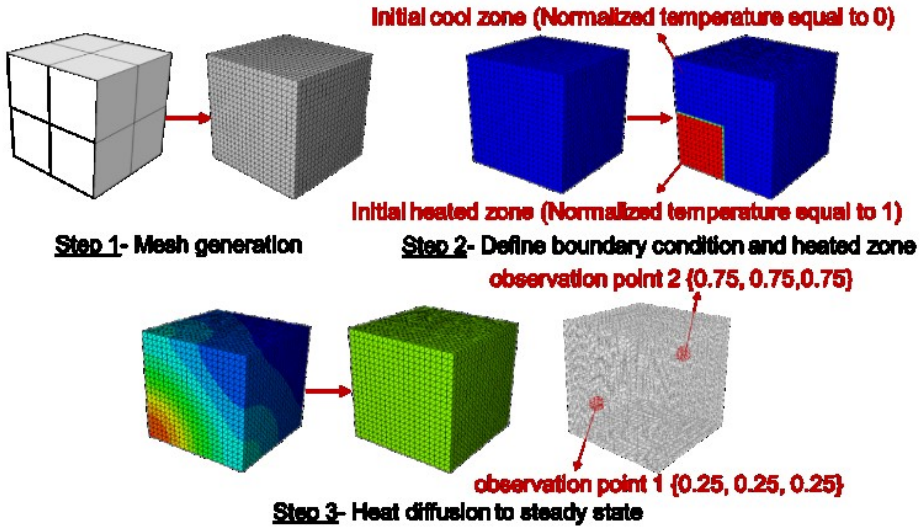

Figure 10. The three steps of FEA towards the error calculation and verification with the analytical method.

b. Comparison of the Graph Theory and Finite Element Analysis Solutions.

Continuing with our study of heat diffusion for the cuboid geometry, we now compare the graph theoretic and finite element (FE) analysis solutions. The FE analysis study is implemented in Abaqus software. The FE analysis process is divided into three steps as shown in Figure 10.

Step 1: *Mesh generation in finite element analysis.*

We applied both tetrahedral and regular grid (hexahedron) meshes on the cube. It was observed that tetrahedral mesh performs better than regular grid mesh in terms of accuracy.

Step 2: *Boundary condition and initial heat condition in finite element analysis.*

Identical boundary conditions as in case of the analytical method are applied herewith, i.e., the heat disperses through the part, and the cube is perfectly insulated (Neumann boundary condition). As with the analytical method, the material properties such as thermal conductivity, specific heat, and density of material in this method are considered to be equal to 1 unit.

Step 3: *Heat diffusion to steady state in finite element analysis.*

The heat diffuses through the cube volume until a steady state condition is reached. Table 2 reports a comparison between the total calculation time and number of nodes for FE analysis and graph theory. The number of nodes in FE analysis was chosen to give approximately the same error as graph theory. The result shows that the proposed graph theoretic approach gives comparable accuracy at within a fraction of the computational time taken by FE analysis.

Table 2. Comparison of FEA and Graph Theoretic Approach Based on the Total Computational Time and Accuracy.

SMAPE (Error)	Graph theoretic approach		Tetrahedral FE analysis		Regular Grid FE analysis	
	Nodes	Time (sec)	Nodes	Time (sec)	Nodes	Time (sec)
10%	80	1	1,200	190	9,000	380
7%	800	2	12,000	660	158,500	9,000
~ 5%	8,000	237	76,000	3,540	1,000,000	43,000

4.2 Verification of the Graph Theory Approach with Goldak's Finite Element Analysis Solution in LPBF.

a. Finite Element Analysis of LPBF Parts based on Goldak's Moving Heat Source Model.

We now compare the solutions resulting from the graph theoretic approach with FE analysis for three test objects in LPBF scenario using Goldak's model. Goldak *et al.* extended the pioneering work of Rosenthal [61] to predict the heat flux in welding process [56, 57]. Goldak *et al.* considered a 3D moving heat source model with an ellipsoidal, Gaussian density distribution as opposed to Rosenthal's 1D moving point heat source.

Goldak's model has been adapted for thermal modeling in AM process, e.g., in LPBF with the laser considered a 3D Gaussian distributed moving heat source [62]. We use Goldak's model in an FE analysis framework (Abaqus) with an element birth-and-death technique to simulate the LPBF process; the DFLUX subroutine in Abaqus is leveraged to model the characteristics of the laser. The Gaussian distributed laser heat source is written as,

$$Q(x,y,z) = \frac{PA}{2\pi\sigma^2} \mathrm{e}^{-\frac{d^2}{2\sigma^2}} \tag{19}$$

Where, Q is the volume heat power density [W/mm^3], P is the laser power [W], A is the constant of absorptivity set to 0.7, σ is the standard deviation (quarter of the beam diameter in m) and d [m] is the radial distance of a point from the center of the beam [63]. The term Q is identical to the energy density term E_v in Eqn. (1). The simplest form of the transient heat conduction, identical to Eqn. (1), is used in this study, with E_v set equal to Q. In this mode, conduction plays the main role in transferring the applied heat through the part and substrate. The radiative heat losses are not considered in this study to make an equitable comparison with the graph theoretic approach.

Description of the Boundary Conditions and Test Part Geometries

The LPBF of two C-shaped test parts (Figure 11(a), (b)) and a pyramid shaped test part (Figure 11(c)) are simulated (separately, one at a time) on top of a build plate with the dimension of 100 × 20 × 10 mm having identical material as the test parts (Titanium alloy Ti6Al4V). The C-shaped part in Figure 11(a) has an overhang geometry akin to the knee implant in Figure 3. The second C-shaped part, Figure 11(b), has the overhang area provided with thick supports. Figure 12 shows the scanning strategy used for these parts in the LPBF simulation. The hatches (the linear scan pattern of the laser) are defined along y-axis and layers along the z-axis.

The laser is simulated to move along x-axis and traces a linear hatch pattern in each layer. Based on the width of each layer, the number of hatches per layer remain constant in the two C-shaped parts, but vary in the pyramid test part, i.e., 20 hatches in the first layer, 18 hatches in second layer, and so on, until finally only one hatch is needed in layer 20. The hatch spacing, and layer thickness are 0.5 mm and 0.2 mm for the two C-shaped parts, and pyramid, respectively.

The layer thickness is purposely made exceedingly coarse to facilitate computation, and should ideally be termed as a super layer – each super layer consists of 20 individual layers of size 0.025 mm (25 μm) for the C-shaped parts and 8 super layers for the pyramid part. These super layers are consolidated in an identical manner for the finite element and proposed graph theoretic approach. The titanium alloy powder material Ti6Al4V is considered for both the part and the build plate.

The material properties and printing conditions are reported in Table 3, based on the literature [59, 62]. The parameters for the graph theoretic approach were set as follows based on offline heuristic tuning: ϵ = 1.8 mm; g = 2 × 10^6 m^{-2} and 50 nodes are sampled per hatch in the C-shaped parts. These parameters for the pyramid are: ϵ = 0.25 mm; g = 2 × 10^6 m^{-2} and 40 nodes are sampled per hatch. The temperature history at two locations on the bottom for the C-shaped part and one location on the bottom for the pyramid were recorded over the complete simulation run, analogous to the presence of thermocouple sensors affixed to the part at these locations.

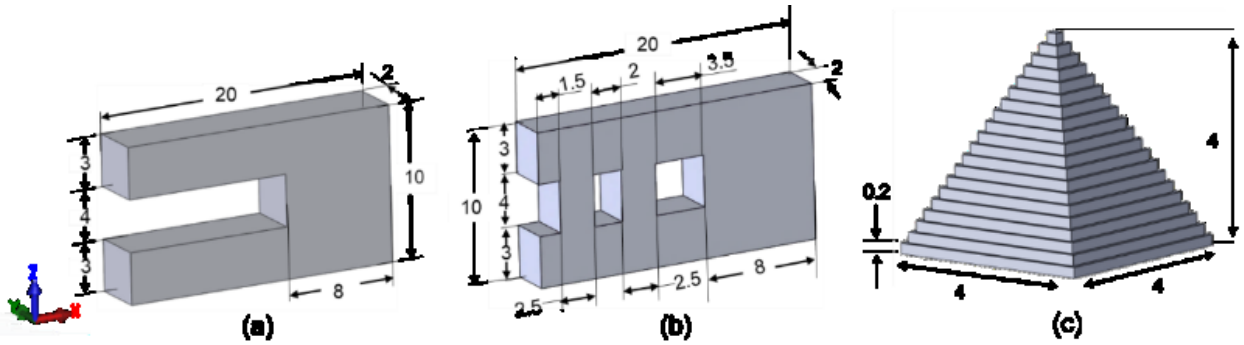

Figure 11. (a) C-shaped, (b) C-shaped with support and (c) pyramid dimensions in millimeter (mm).

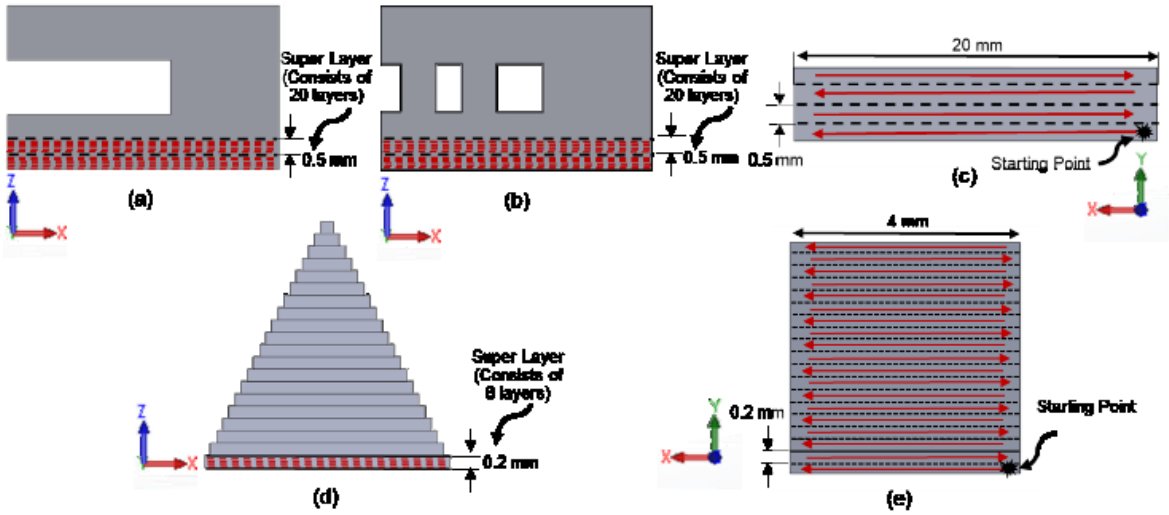

Figure 12. (a) Side view of C-shaped part, (b) Side view of C-shaped part with supports (c) Scanning strategy of the two C-shaped parts from top view, (d) Side view of pyramid part, (e) Scanning strategy of pyramid part from its top view.

Table 3. *Materials and Process Parameters for the FE analysis (Abaqus) and Netfabb Simulation*.

Parameters	Values	
	C-Shaped Parts	Pyramid
Layer Thickness (mm)	0.025	
Super Layer Thickness (mm)	0.5 (20 layers)	0.2 (8 layers)
Hatch thickness (mm)	0.5	0.2
Beam Diameter (mm)	0.5	0.2
Laser Power, P (W)	200	
Scanning Speed (mm/s)	200	
Thermal Conductivity, k (W/m. K)	20	
Thermal Absorptivity Coefficient, A	0.7	
Thermal Diffusivity, α (m^2/s)	7×10^{-6}	
Density, ρ (kg/m^3)	4,300	
Specific Heat, C_p (J/kg·K)	650	
Ambient Temperature, T_∞ (K)	298	

b. Heat Flux in C-shaped Part without Supports

For both the C-shaped parts, the heat flux is observed at two locations which are at a distance of 1 mm from the left edge and 1 mm from the right edge of the part, as demarcated in the inset of Figure 13(b) and (c); both are located 1 mm deep from the front edge of the part. We observe that the trends obtained from Figure 13(b) and (c) for both the FE analysis and graph-based methods are closely correlated. More pertinently as reported in Table 4 the simulation time of C-shaped part for the FE approach (on Abaqus) was close to 200 minutes (>3 hrs.) on a dual core of Intel® Core™ i7-6700 CPU @3.40GHz, 32GB RAM. While the computation time for the graph theoretic approach was less than 200 seconds on the same machine with Matlab.

The temperature trends observed in the C-shaped part is explained on partitioning the part geometry into three sections T1, T2 and T3 as demarcated in Figure 13(a). In Figure 13(b) the spikes in section T1 correspond to the locations where the laser is directly (in the vertical direction) above the position of the left measurement point. In section T2, the laser no longer passes over the location of the measurement point leading to the observed precipitous drop. In section T3, given the impeded conductivity of the powder surrounding the overhang, the temperature does not increase, though the laser does pass directly over the sensor location.

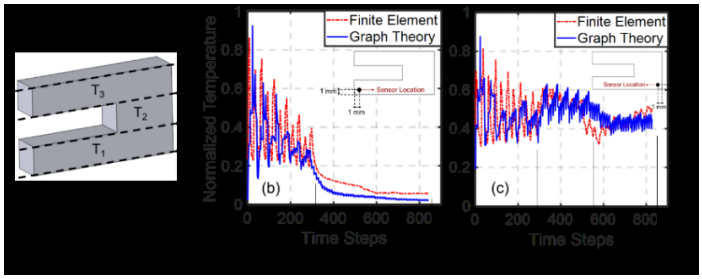

Figure 13. (a) The C-shaped part and three different section of the part, the heat flux trends observed at two locations on the part, in the left (b) and right (c) corner, respectively corresponding to the three part sections marked in (a).

In Figure 13(c), the spikes in section T1 of the part correspond to the location where the laser passes over the measurement point on the right. In area T2, the increase in temperature can be attributed to two reasons: (i) in section T2 of the part, the laser passes frequently and directly above the sensor location, and (ii) section T2 is surrounded by a large volume of powder that hinders the flow of heat through it. Lastly, in section T3, the temperature begins to rise again due to the constrained heat flux in the overhang feature, which is isolated through the bulk section of the part. Furthermore, the trends obtained are in accordance with those expected for parts with overhang features as shown in Figure 3; the heat in overhang features is constrained in the C-shaped part because of the lack of sufficient conductivity of the powder surrounding the overhang sections.

c. Heat Flux in C-shaped Part with Supports

Based on the heat distribution results from the C-shaped part (Figure 13) which showed that heat was constrained in the overhang section, it was hypothesized that designing supports (under the overhang) would provide a pathway for the heat to dissipate into the build plate. Accordingly, the C-shaped part was modified as shown in Figure 11(b). We note that the cross section of the support is designed with the same thickness as the rest of the part. The build process was simulated using the identical settings for the FE analysis and graph theoretic approach (Figure 12).

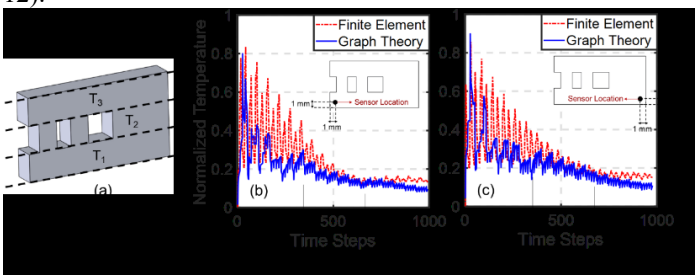

Figure 14. (a) The C-shaped part from Figure 13 is modified with two supports to provide a path for the heat in the overhang section to dissipate. The heat flux trends observed at two locations on the part, in the left (b) and right (c) corner, respectively, corresponding to the three sections marked in (a).

The heat is measured at the two locations, identical to the previous case. Juxtaposing Figure 14(b) and (c) against, Figure 13(b) and (c), respectively, it is evident that placing the supports under the overhang section aids in the dissipation of heat. For instance, in Figure 14(b), the temperature reduction at the end of section T1 is not precipitous as in Figure 13(b). Therefore, the possibility of thermal stress-related deformation and cracking are potentially minimized. Further, this result can will lead to an understanding of the impact of supports on the heat flux, and thus open a path to the use supports as a design feature to not only to anchor the part, but also as a means to conduct the heat trapped in a narrow area, such as an overhang.

d. Heat Flux in a Pyramid-shaped Part

Figure 15 delineates the temperature history at an measurement point which is located in layer 3 for the pyramid shaped part. Each spike in Figure 15 corresponds the layer in which the laser passes over the measurement point. The height of spikes becomes ever smaller as the laser moves to the subsequent layers, due to proportionally smaller energy applied per layer, and also because the bottom layers have a larger area, which facilitates heat dissipation.

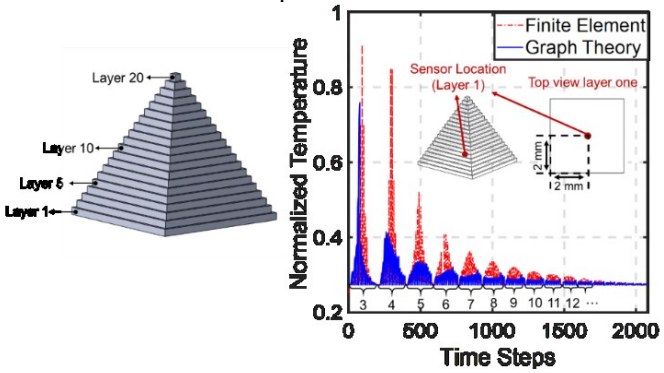

Figure 15. The temperature profile one observation point which is located at the middle of layer one, and the spikes observed while the laser moves from layer 3 to layer 20.

e. Comparison of Temperature History and Heat Distribution Results from Finite Element Analysis (Abaqus) and a Commercial Software (Netfabb) with Graph Theoretic Solution

The computation time and error (SMAPE, Eqn. (18)) between the heat flux trends obtained from the graph theory and FE methods for the three parts are reported in Table 4.

These results indicate that the heat flux trends predicted by the graph theory and FE-based approaches are within 15%. More pertinently, the computation time with graph theory is a fraction of that taken by FE analysis. In our forthcoming research, we will attempt to further improve this result by including radiative effects.

Lastly, the heat distribution results from the last layer of Goldaks's FE model, solution from the commercial Netfabb's package, and graph theoretic simulations are juxtaposed pictorially in Figure 16. The color bars represent normalized temperature between 0 and 1. From Figure 16, it is evident that the temperature distribution captured by the graph theoretic approach closely resembles those derived from the Goldaks's FE model and Autodesk's Netfabb.

Table 4. Comparison of Calculation Time and Symmetric Mean Absolute Percentage Error (SMAPE) for FE analysis (Abaqus) and Graph Theory Solutions for the three test parts shown in Figure 13 through Figure 15.

Part	Graph Theoretic Computational Time (min.)	FE-analysis (Abaqus) Computational Time (min.)	SMAPE (Error)
C-shaped part Left side observation point, Figure 13(b)	3 (6,000 nodes)	200 (9,500 nodes)	11.24%
C-shaped part Right side observation point, Figure 13(c)			10.97%
C-shaped part with supports Left side observation point, Figure 14(b)	3 (6,000 nodes)	208 (11,200 nodes)	13.64%
C-shaped part with supports Right side observation point, Figure 14(c)			13.33%
Pyramid, Figure 15	66 (8,000 nodes)	1380 (73,000 nodes)	6.72%

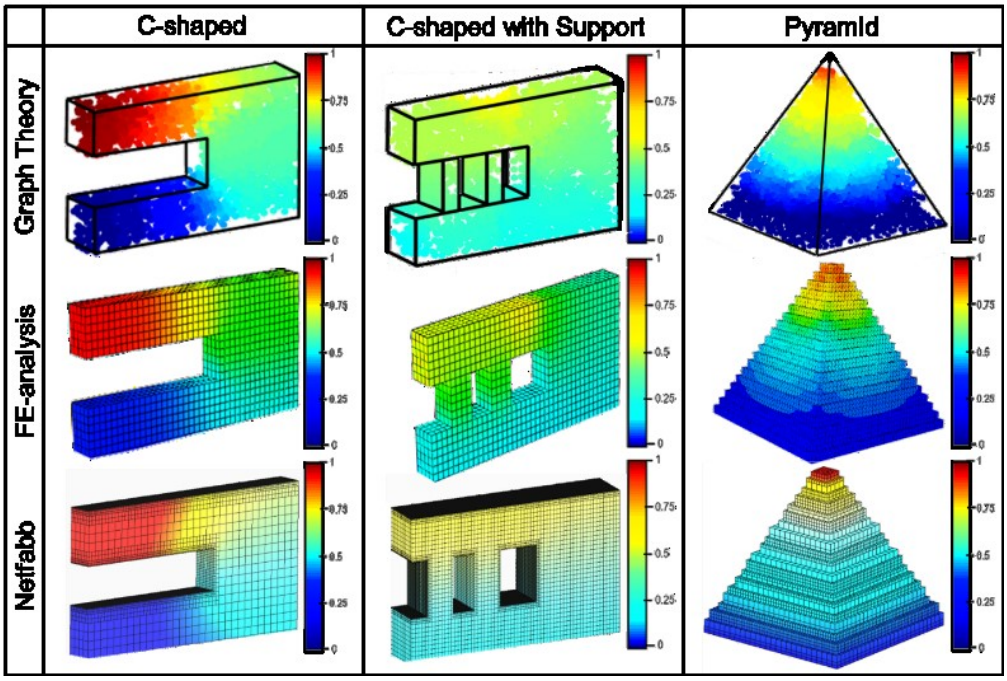

Figure 16. Heat distribution of three parts which is compared by three different methods; graph theory, FE analysis (Abaqus) and commercial software (Netfabb).

5 Conclusions and Avenues for Future Work

In this work, we developed and applied a novel graph theory-based approach to predict the instantaneous spatial distribution of heat, i.e., the direction and magnitude of heat flow (heat flux) or temperature history, in metal parts as they are being printed layer-upon-layer using additive manufacturing (AM) processes, such as laser powder bed fusion (LPBF). The approach relies on converting a part geometry into discrete nodes and connecting them to form a network graph, and subsequently studying the heat diffusion behavior over the network graph embedded in the part. The key result of this work is that the eigenvectors ($\boldsymbol{\phi}$) and eigenvalues ($\boldsymbol{\Lambda}$) derived from Laplacian ($\mathbf{L}$) of the network graph solves the heat diffusion equation (Eqn. (1) and Eqn. (2)), which governs the temperature history in AM processes. Simulations of a LPBF process are compared with FE analysis moving heat source model based on the work of Goldak [56, 57]. Specific results are:

(1) The discrete approximation of the heat flux trends obtained using the graph Laplacian eigenvectors and eigenvalues is observed to closely agree with results from the FE-based approach. The computation time to estimate the heat flux with the graph theoretic approach for the three test parts studied was significantly faster compared to FE-based approach (Abaqus). For instance, for a C-shaped part, the simulation time was 3 minutes using the graph theoretic approach compared to over the 3 hours with FE analysis (Abaqus).

(2) The error in the FE and graph theoretic solutions for the same part was within 15%. The graph-based results were

further compared qualitatively with Autodesk Netfabb solution, and showed similar trends. While this work presents the first foray into using graph theory for modeling the part-level thermal phenomena in metal AM, the experimental validation with temperature and deformation measurements term of deformation estimation aspect remains to be addressed. The experimental validation of the approach is also essential to calibrate the parameters, such as, neighborhood distance (ϵ), and gain factor (g) in Eqn. (4) and Eqn. (11), respectively.

In our forthcoming works in this area we will also endeavor to answer the following questions:

- What is the effect of the process conditions, such as laser power, velocity, and scan strategy on the heat flux, part deformation and microstructural evolution in metal AM parts?
- What is the true temperature instead of the normalized temperature? What experimental strategy should be used to calibrate the adjustable parameters, ϵ and g?

ACKNOWLEDGEMENTS

One of the authors (PKR) thanks the NSF for funding his research through the following grants CMMI-1719388, CMMI-1739696 and CMMI-1752069 (CAREER) at University of Nebraska-Lincoln. Specifically, the concept of using spectral graph theory for modeling in metal additive manufacturing applications was funded through CMMI-1752069 towards a *correct-as-you-build* smart additive manufacturing paradigm.
The authors additionally thank Autodesk for providing complimentary educational licenses for the Netfabb simulation program. The help of Mr. Aniruddha Gaikwad in coding the approach in Matlab is gratefully acknowledged by the authors.

APPENDIX.
SOLUTION OF THE HEAT EQUATION USING GRAPH THEORY

In this Appendix the graph-based solution of the discrete heat diffusion equation is developed. The discrete heat diffusion equation has the form,

$$\frac{\partial \mathbf{T}}{\partial t} + \alpha \mathbf{L}\mathbf{T} = 0$$

subject to the initial condition,

$$\mathbf{T}(x, y, z, t = 0) = \mathbf{T_o}(x, y, z)$$

Here, **T** is a column vector for temperature at each of M nodes in the domain and **L** is the [M × M] Laplacian matrix. For boundary conditions of type Dirichlet, Neumann, and Robin, (types 1, 2 and 3, boundary conditions respectively), it is shown by Saito that the eigenvalues (Λ) of the discrete Laplacian operator are discrete and non-negative, and the eigenvectors are orthogonal, i.e., $\langle \boldsymbol{\phi_i}, \boldsymbol{\phi_j} \rangle = 0$, assuming that the domain of the Laplacian is bounded, connected and compact [64]. The particular form of the Laplacian matrix discussed here, as described in (Eqn. (4)– Eqn. (10)), is diagonally dominant and symmetric, i.e., positive semidefinite. Accordingly, the orthogonality of eigenvectors ($\boldsymbol{\phi}$) and non-negativity of eigenvalues (Λ) of the Laplacian matrix (**L**) is preserved [58].

The eigenvectors and eigenvalues of the Laplacian matrix are found with standard matrix methods, and satisfy the following eigenvalue equation,

$$\mathbf{L}\boldsymbol{\phi} = \boldsymbol{\phi}\boldsymbol{\Lambda}$$

Here $\boldsymbol{\phi}$ is the right eigenvector matrix in which each column contains one of M eigenvectors, and $\boldsymbol{\Lambda}$ is a diagonal matrix containing non-negative eigenvalues ranked in order from the smallest in row 1 to the largest in row M. Because the transpose of an orthogonal matrix is the same as its inverse, that is, $\boldsymbol{\phi}^{-1} = \boldsymbol{\phi}'$, and $\boldsymbol{\phi}\,\boldsymbol{\phi}' = \mathbf{I}$, then the above eigenvalue equation may be post multiplied by $\boldsymbol{\phi}'$ to obtain,

$$\mathbf{L} = \boldsymbol{\phi}\boldsymbol{\Lambda}\boldsymbol{\phi}'$$

Replacing this relationship into the discrete heat diffusion equation we obtain,

$$\frac{\partial \mathbf{T}}{\partial t} + \alpha(\boldsymbol{\phi}\boldsymbol{\Lambda}\boldsymbol{\phi}')\,\mathbf{T} = 0$$

This first order ordinary differential equation has solution

$$\mathbf{T} = e^{-\alpha g(\boldsymbol{\phi}\boldsymbol{\Lambda}\boldsymbol{\phi}')t}\ \mathbf{T_o} \qquad (20)$$

Where g [m^{-2}] is a gain factor that we have added to calibrate the solution and adjust the units. Hence, the heat equation solution contains the eigenvectors and eigenvalues of the graph Laplacian **L.** This formal matrix solution gives the temperature vector **T**, which contains a value for every spatial node, subject to the initial condition vector $\mathbf{T_o}$. This solution can be simplified for improved computational efficiency by considering the Taylor Series expansion of the term $e^{-\alpha g(\boldsymbol{\phi}\boldsymbol{\Lambda}\boldsymbol{\phi}')t}$, and substituting $\boldsymbol{\phi}\,\boldsymbol{\phi}' = \mathbf{I}$, as shown by Zhang *et al.* and Bai *et al.* as follows [50, 65],

$$e^{-\alpha g(\boldsymbol{\phi}\boldsymbol{\Lambda}\boldsymbol{\phi}')t} = I + \frac{(-\alpha g(\boldsymbol{\phi}\boldsymbol{\Lambda}\boldsymbol{\phi}')t)}{1!} + \frac{(-\alpha g(\boldsymbol{\phi}\boldsymbol{\Lambda}\boldsymbol{\phi}')t)^2}{2!} + \frac{(-\alpha g(\boldsymbol{\phi}\boldsymbol{\Lambda}\boldsymbol{\phi}')t)^3}{3!} + \cdots$$

$$e^{-\alpha g(\boldsymbol{\phi}\boldsymbol{\Lambda}\boldsymbol{\phi}')t} = I - \alpha g t\frac{\boldsymbol{\phi}\boldsymbol{\Lambda}\boldsymbol{\phi}'}{1!} + \alpha^2 g^2 t^2 \frac{(\boldsymbol{\phi}\boldsymbol{\Lambda}\boldsymbol{\phi}')(\boldsymbol{\phi}\boldsymbol{\Lambda}\boldsymbol{\phi}')}{2!} - \alpha^3 g^3 t^3 \frac{(\boldsymbol{\phi}\boldsymbol{\Lambda}\boldsymbol{\phi}')(\boldsymbol{\phi}\boldsymbol{\Lambda}\boldsymbol{\phi}')(\boldsymbol{\phi}\boldsymbol{\Lambda}\boldsymbol{\phi}')}{3!} + \cdots$$

$$e^{-\alpha g(\boldsymbol{\phi}\boldsymbol{\Lambda}\boldsymbol{\phi}')t} = I - \frac{\boldsymbol{\phi}\boldsymbol{\Lambda}\alpha g t\boldsymbol{\phi}'}{1!} + \frac{\boldsymbol{\phi}(\boldsymbol{\Lambda}\alpha g t)^2\boldsymbol{\phi}'}{2!} - \frac{\boldsymbol{\phi}(\boldsymbol{\Lambda}\alpha g t)^3\boldsymbol{\phi}'}{3!} + \cdots$$

Thus, replacing $e^{-\alpha g(\boldsymbol{\phi}\boldsymbol{\Lambda}\boldsymbol{\phi}')t} = \boldsymbol{\phi}e^{-\alpha g\boldsymbol{\Lambda}t}\boldsymbol{\phi}'$ in Eqn. (20) gives,

$$\mathbf{T} = \boldsymbol{\phi}e^{-\alpha g\boldsymbol{\Lambda}t}\boldsymbol{\phi}'\,\mathbf{T_o} \qquad (21)$$

This expression is the key to the computational efficiency of our approach, because the temperature at successive time steps is computed by matrix multiplication only. In contrast, finite-element or finite-difference methods require a matrix inversion at every time step, at great computational cost.

REFERENCES

[1] Schmidt, M., Merklein, M., Bourell, D., Dimitrov, D., Hausotte, T., Wegener, K., Overmeyer, L., Vollertsen, F., and Levy, G. N., 2017, "Laser based additive manufacturing in industry and academia," CIRP Annals, **66**(2), pp. 561-583.

[2] Gibson, I., Rosen, D. W., and Stucker, B., 2010, Additive manufacturing technologies: rapid prototyping to direct digital manufacturing, Springer,

[3] Sames, W. J., List, F., Pannala, S., Dehoff, R. R., and Babu, S. S., 2016, "The metallurgy and processing science of metal additive manufacturing," International Materials Reviews, **61**(5), pp. 315-360.

[4] Gu, D. D., Meiners, W., Wissenbach, K., and Poprawe, R., 2012, "Laser additive manufacturing of metallic components: materials, processes and mechanisms," International Materials Reviews, **57**(3), pp. 133-164.

[5] Sames, W. J., List, F. A., Pannala, S., Dehoff, R. R., and Babu, S. S., 2016, "The metallurgy and processing science of metal additive manufacturing," International Materials Reviews, **61**(5), pp. 315-360.

[6] Das, S., Bourell, D. L., and Babu, S. S., 2016, "Metallic materials for 3D printing," MRS Bulletin, **41**(10), pp. 729-741.

[7] Gibson, I., Rosen, D. W., and Stucker, B., "Additive manufacturing technologies. 2010," Google Scholar

[8] Tofail, S. A. M., Koumoulos, E. P., Bandyopadhyay, A., Bose, S., O'Donoghue, L., and Charitidis, C., 2018, "Additive manufacturing: scientific and technological challenges, market uptake and opportunities," Materials Today, **21**(1), pp. 22-37.

[9] Khoda, B., Benny, T., Rao, P. K., Sealy, M. P., and Zhou, C., 2017, "Applications of Laser-Based Additive Manufacturing," Laser-Based Additive Manufacturing of Metal Parts, CRC Press, pp. 253-298.

[10] Badiru, A. B., Valencia, V. V., and Liu, D., 2017, Additive manufacturing handbook: product development for the defense industry, CRC Press,

[11] Bauereiß, A., Scharowsky, T., and Körner, C., 2014, "Defect generation and propagation mechanism during additive manufacturing by selective beam melting," Journal of Materials Processing Technology, **214**(11), pp. 2522-2528.

[12] Liu, Q. C., Elambasseril, J., Sun, S. J., Leary, M., Brandt, M., and Sharp, P. K., 2014, "The effect of manufacturing defects on the fatigue behaviour of Ti-6Al-4V specimens fabricated using selective laser melting," Advanced Materials Research, Trans Tech Publ, pp. 1519-1524.

[13] Gorelik, M., 2017, "Additive manufacturing in the context of structural integrity," International Journal of Fatigue, **94, Part 2**, pp. 168-177.

[14] Seifi, M., Gorelik, M., Waller, J., Hrabe, N., Shamsaei, N., Daniewicz, S., and Lewandowski, J. J., 2017, "Progress Towards Metal Additive Manufacturing Standardization to Support Qualification and Certification," JOM, **69**(3), pp. 439-455.

[15] Lewandowski, J. J., and Seifi, M., 2016, "Metal additive manufacturing: a review of mechanical properties," Annual Review of Materials Research, **46**, pp. 151-186.

[16] DebRoy, T., Wei, H. L., Zuback, J. S., Mukherjee, T., Elmer, J. W., Milewski, J. O., Beese, A. M., Wilson-Heid, A., De, A., and Zhang, W., 2018, "Additive manufacturing of metallic components – Process, structure and properties," Progress in Materials Science, **92**, pp. 112-224.

[17] Foteinopoulos, P., Papacharalampopoulos, A., and Stavropoulos, P., 2018, "On thermal modeling of Additive Manufacturing processes," CIRP Journal of Manufacturing Science and Technology, **20**, pp. 66-83.

[18] Kruth, J. P., Froyen, L., Van Vaerenbergh, J., Mercelis, P., Rombouts, M., and Lauwers, B., 2004, "Selective laser melting of iron-based powder," Journal of Materials Processing Technology, **149**(1), pp. 616-622.

[19] Everton, S. K., Hirsch, M., Stravroulakis, P., Leach, R. K., and Clare, A. T., 2016, "Review of in-situ process monitoring and in-situ metrology for metal additive manufacturing," Materials & Design, **95**, pp. 431-445.

[20] Maskery, I., Aboulkhair, N. T., Corfield, M. R., Tuck, C., Clare, A. T., Leach, R. K., Wildman, R. D., Ashcroft, I. A., and Hague, R. J. M., 2016, "Quantification and characterisation of porosity in selectively laser melted Al–Si10–Mg using X-ray computed tomography," Materials Characterization, **111**, pp. 193-204.

[21] Hadadzadeh, A., Amirkhiz, B. S., Li, J., and Mohammadi, M., 2018, "Columnar to equiaxed transition during direct metal laser sintering of AlSi10Mg alloy: Effect of building direction," Additive Manufacturing, **23**, pp. 121-131.

[22] Markl, M., and Körner, C., 2016, "Multiscale Modeling of Powder Bed–Based Additive Manufacturing," Annual Review of Materials Research, **46**(1), pp. 93-123.

[23] Bourell, D., Kruth, J. P., Leu, M., Levy, G., Rosen, D., Beese, A. M., and Clare, A., 2017, "Materials for additive manufacturing," CIRP Annals, **66**(2), pp. 659-681.

[24] Seifi, M., Salem, A., Beuth, J., Harrysson, O., and Lewandowski, J. J., 2016, "Overview of Materials Qualification Needs for Metal Additive Manufacturing," JOM, **68**(3), pp. 747-764.

[25] O'Regan, P., Prickett, P., Setchi, R., Hankins, G., and Jones, N., 2016, "Metal Based Additive Layer Manufacturing: Variations, Correlations and Process Control," Procedia Computer Science, **96**, pp. 216-224.

[26] Huang, Y., Leu, M. C., Mazumder, J., and Donmez, A., 2015, "Additive Manufacturing: Current State, Future Potential, Gaps and Needs, and Recommendations," Transactions of the ASME, Journal of Manufacturing Science and Engineering, **137**(1), p. 014001.

[27] Huang, Y., and Leu, M., 2013, "Frontiers of Additive Manufacturing Research and Education—Report of NSF Additive Manufacturing Workshop," National Science Foundation, Arlington, VA.

[28] 2013, Report to the National Institute of Standards and Technology: Measurement Science Roadmap for Metal-Based Additive Manufacturing, Energetics Corporation, Gaithersburg, MD

[29] Cheng, B., and Chou, K., 2015, "Deformation Evaluation of Part Overhang Configurations in Electron Beam Additive

Manufacturing," ASME 2015 International Manufacturing Science and Engineering Conference, American Society of Mechanical Engineers, pp. V001T002A072-V001T002A072.
[30] Edgar, T., Davis, J., and Burka, M., 2015, "NSF Workshop on Research needs in Advanced Sensors, Controls, Platforms, and Modeling (ASCPM) for Smart Manufacturing ", National Science Foundation, Atlanta, GA.
[31] Simpson, T. W., Williams, C. B., and Hripko, M., 2017, "Preparing industry for additive manufacturing and its applications: Summary & recommendations from a National Science Foundation workshop," Additive Manufacturing, **13**, pp. 166-178.
[32] Liu, Q. C., Elambasseril, J., Sun, S. J., Leary, M., Brandt, M., and Sharp, P. K., 2014, "The Effect of Manufacturing Defects on the Fatigue Behaviour of Ti-6Al-4V Specimens Fabricated Using Selective Laser Melting," Advanced Materials Research, **891-892**, pp. 1519-1524.
[33] Gu, H., Gong, H., Pal, D., Rafi, K., Starr, T., and Stucker, B., 2013, "Influences of energy density on porosity and microstructure of selective laser melted 17-4PH stainless steel," 2013 Solid Freeform Fabrication Symposium.
[34] Gong, H., Rafi, K., Gu, H., Starr, T., and Stucker, B., 2014, "Analysis of defect generation in Ti–6Al–4V parts made using powder bed fusion additive manufacturing processes," Additive Manufacturing, **1-4**, pp. 87-98.
[35] Gong, H., Rafi, K., Starr, T., and Stucker, B., 2012, "Effect of defects on fatigue tests of as-built Ti-6Al-4V parts fabricated by selective laser melting," Solid freeform fabrication symposium, University of Texas Austin, Texas, pp. 499-506.
[36] Montazeri, M., and Rao, P., 2018, "Sensor-Based Build Condition Monitoring in Laser Powder Bed Fusion Additive Manufacturing Process Using a Spectral Graph Theoretic Approach," Journal of Manufacturing Science and Engineering, **140**(9), pp. 091002-091002-091016.
[37] Fox, J. C., Moylan, S. P., and Lane, B. M., 2016, "Effect of process parameters on the surface roughness of overhanging structures in laser powder bed fusion additive manufacturing," Procedia CIRP, **45**, pp. 131-134.
[38] Strano, G., Hao, L., Everson, R., and Evans, K., 2013, "A new approach to the design and optimisation of support structures in additive manufacturing," The International Journal of Advanced Manufacturing Technology, **66**(9-12), pp. 1247-1254.
[39] Thomas, D., 2009, "The development of design rules for selective laser melting," Ph.D. Dissertation, University of Wales.
[40] Montazeri, M., Yavari, R., Rao, P., and Boulware, P., 2018, "In-Process Monitoring of Material Cross-Contamination Defects in Laser Powder Bed Fusion," Journal of Manufacturing Science and Engineering, **140**(11), pp. 111001-111001-111019.
[41] Denlinger, E. R., Irwin, J., and Michaleris, P., 2014, "Thermomechanical Modeling of Additive Manufacturing Large Parts," Journal of Manufacturing Science and Engineering, **136**(6), pp. 061007-061007-061008.
[42] Bandyopadhyay, A., and Traxel, K. D., 2018, "Invited Review Article: Metal-additive manufacturing—Modeling strategies for application-optimized designs," Additive Manufacturing
[43] DebRoy, T., Wei, H., Zuback, J., Mukherjee, T., Elmer, J., Milewski, J., Beese, A., Wilson-Heid, A., De, A., and Zhang, W., 2018, "Additive manufacturing of metallic components–process, structure and properties," Progress in Materials Science, **92**, pp. 112-224.
[44] Denlinger, E. R., Gouge, M., and Michaleris, P., 2018, Thermo-Mechanical Modeling of Additive Manufacturing, Butterworth-Heinemann,
[45] Francois, M. M., Sun, A., King, W. E., Henson, N. J., Tourret, D., Bronkhorst, C. A., Carlson, N. N., Newman, C. K., Haut, T., Bakosi, J., Gibbs, J. W., Livescu, V., Vander Wiel, S. A., Clarke, A. J., Schraad, M. W., Blacker, T., Lim, H., Rodgers, T., Owen, S., Abdeljawad, F., Madison, J., Anderson, A. T., Fattebert, J. L., Ferencz, R. M., Hodge, N. E., Khairallah, S. A., and Walton, O., 2017, "Modeling of additive manufacturing processes for metals: Challenges and opportunities," Current Opinion in Solid State and Materials Science, **21**(4), pp. 198-206.
[46] Zeng, K., Pal, D., Gong, H. J., Patil, N., and Stucker, B., 2015, "Comparison of 3DSIM thermal modelling of selective laser melting using new dynamic meshing method to ANSYS," Materials Science and Technology, **31**(8), pp. 945-956.
[47] Cheng, B., Shrestha, S., and Chou, Y. K., 2016, "Stress and deformation evaluations of scanning strategy effect in selective laser melting," ASME 2016 11th International Manufacturing Science and Engineering Conference, American Society of Mechanical Engineers, pp. V003T008A009-V003T008A009.
[48] Williams, R. J., Davies, C. M., and Hooper, P. A., 2018, "A Pragmatic Part Scale Model for Residual Stress and Distortion Predictionin Powder Bed Fusion," Additive Manufacturing
[49] Michaleris, P., 2014, "Modeling metal deposition in heat transfer analyses of additive manufacturing processes," Finite Elements in Analysis and Design, **86**, pp. 51-60.
[50] Peng, H., Ghasri-Khouzani, M., Gong, S., Attardo, R., Ostiguy, P., Gatrell, B. A., Budzinski, J., Tomonto, C., Neidig, J., Shankar, M. R., Billo, R., Go, D. B., and Hoelzle, D., 2018, "Fast prediction of thermal distortion in metal powder bed fusion additive manufacturing: Part 1, a thermal circuit network model," Additive Manufacturing, **22**, pp. 852-868.
[51] Ganeriwala, R., and Zohdi, T. I., 2014, "Multiphysics modeling and simulation of selective laser sintering manufacturing processes," Procedia CIRP, **14**, pp. 299-304.
[52] Ganeriwala, R., and Zohdi, T. I., 2016, "A coupled discrete element-finite difference model of selective laser sintering," Granular Matter, **18**(2), p. 21.
[53] Solomon, J., 2015, "PDE approaches to graph analysis," arXiv preprint arXiv:1505.00185
[54] Belkin, M., Sun, J., and Wang, Y., 2008, "Discrete laplace operator on meshed surfaces," Proceedings of the twenty-fourth annual symposium on Computational geometry, ACM, pp. 278-287.
[55] Zhang, F., and Hancock, E. R., 2008, "Graph spectral image smoothing using the heat kernel," Pattern Recognition, **41**(11), pp. 3328-3342.

[56] Silling, S. A., and Askari, E., 2005, "A meshfree method based on the peridynamic model of solid mechanics," Computers & Structures, **83**(17), pp. 1526-1535.
[57] Chen, Z., Niazi, S., Zhang, G., and Bobaru, F., 2017, "Peridynamic Functionally Graded and Porous Materials: Modeling Fracture and Damage," Handbook of Nonlocal Continuum Mechanics for Materials and Structures, G. Z. Voyiadjis, ed., Springer International Publishing, Cham, pp. 1-35.
[58] Sun, Y.-S., and Li, B.-W., 2010, "Spectral Collocation Method for Transient Conduction-Radiation Heat Transfer," Journal of Thermophysics and Heat Transfer, **24**(4), pp. 823-832.
[59] Rahmati, A. R., and Niazi, S., 2012, "Simulation of microflows using the lattice boltzmann method on nonuniform meshes.," **3**(1), pp. 77-97.
[60] Kondor, R. I., and Lafferty, J. D., 2002, "Diffusion kernels on graphs and other discrete input spaces," Proceedings of the 19th International Conference on Machine Learning.
[61] Goldak, J. A., and Akhlaghi, M., 2005, "Computer simulation of welding processes," Computational Welding Mechanics, pp. 16-69.
[62] Goldak, J., Chakravarti, A., and Bibby, M., 1984, "A new finite element model for welding heat sources," Metallurgical Transactions B, **15**(2), pp. 299-305.
[63] Chung, F. R. K., 1997, Spectral graph theory, American Mathematical Society,
[64] Cole, K. D., Beck, J. V., Haji-Sheikh, A., and Litkouhi, B., 2010, Heat conduction using Green's functions, CRC Press,
[65] Cole, K. D., 2018, "Parallelepiped with insulated boundaries and piecewise initial condition. http://exact.unl.edu/ExactAnlyticalConductionToolbox ".
[66] Nunes, A., 1983, "An extended Rosenthal weld model," Welding journal, **62**(6), pp. 165s-170s.
[67] Karayagiz, K., Elwany, A., Tapia, G., Franco, B., Johnson, L., Ma, J., Karaman, I., and Arróyave, R., 2018, "Numerical and experimental analysis of heat distribution in the laser powder bed fusion of Ti-6Al-4V," IISE Transactions, pp. 1-17.
[68] Rubenchik, A., Wu, S., Mitchell, S., Golosker, I., LeBlanc, M., and Peterson, N., 2015, "Direct measurements of temperature-dependent laser absorptivity of metal powders," Appl. Opt., **54**(24), pp. 7230-7233.
[69] Saito, N., 2013, "Tutorial: Laplacian Eigenfunctions - Foundations and Applications," University of California, Davis, Graduate University for Advanced Studies, National Institute of Fusion Science, Japan.
[70] Bai, X., and Hancock, E. R., 2004, "Heat Kernels, Manifolds and Graph Embedding," Springer Berlin Heidelberg, pp. 198-206.